
Article:
Lewis, T.W.R., Ard, S.G., Viggiano, A.A. et al. (Accepted: 2026) Ion-molecule chemistry relevant to iodine in the upper atmosphere. ACS Earth and Space Chemistry. ISSN: 2472-3452 (In Press)

Ion-molecule chemistry relevant to iodine in the upper atmosphere

Tucker W. R. Lewis, Shaun G. Ard,* Albert A. Viggiano, and Nicholas S. Shuman*
Air Force Research Laboratory, Space Warfare Directorate, Kirtland AFB, NM, USA 87117
Wuhu Feng
National Centre for Atmospheric Science, University of Leeds, Leeds, UK
John M. C. Plane
School of Chemistry, University of Leeds, Leeds, UK

*corresponding author: rvborgmailbox@us.af.mil

Abstract

The kinetics of $I^+ + O_3$, $IO^+ + O_3$, and $IO^+ + O$ are measured using a selected-ion flow tube apparatus over the range 160 – 300 K. Recommended rate constants ($cm^3\ s^{-1}$) are: $I^+ + O_3$ k = $8.9 \pm 1 \times 10^{-10}\ (\frac{T}{200\ K})^{-0.15}$; $IO^+ + O_3$ k = $8 \pm 2 \times 10^{-11}$; $IO^+ + O$ k = $1.6 \pm 0.5 \times 10^{-10}\ (\frac{T}{200\ K})^{-2}$ $cm^3\ s^{-1}$. The $IO^+ + O_3$ reaction yields primarily $IO_2^+ + O_2$, with an upper limit on $I^+ + 2O_2$ of 10^{-11} $cm^3\ s^{-1}$. The results are supported by density functional calculations. A previously reported implementation of iodine chemistry using the Whole Atmosphere Community Climate Model is updated with these values and the chemistry of iodine in the upper atmosphere discussed.

Introduction

Early assessments of the impact of spacecraft and rocket exhaust on the upper atmosphere did not show large cause for alarm.[1,2] However, the dramatic increase in the number of spacecraft operating in low earth orbit requires updating and expanding those assessments.[3–6] Motivated by the development of iodine as a fuel for Hall thrusters powering nanosatellites,[7,8] recent work by some of the present authors highlighted the effects of iodine in the stratosphere and mesosphere/lower thermosphere.[9]

The effects of iodine on the upper atmosphere as well as the lifetimes of iodine-containing neutrals and cations were estimated by extending the Whole Atmosphere Community Climate Model (WACCM) model[10] with the pertinent iodine chemistry. Unfortunately, rather little iodine cation chemistry has been reported in the literature,[11–16] requiring several relevant reaction rate constants involving I^+ and IO^+ to be estimated,

$$I^+ + O_3 \rightarrow IO^+ + O_2 \qquad \Delta_r H^o = -2.02 \pm 0.02\ eV \qquad (1)$$

$$IO^+ + O \rightarrow I^+ + O_2 \qquad \Delta_rH^o = -2.04 \pm 0.02 \text{ eV} \qquad (2a)$$

$$\rightarrow I + O_2^+ \qquad \Delta_rH^o = -0.42 \pm 0.02 \text{ eV} \qquad (2b)$$

$$O_2^+ + I \rightarrow I^+ + O_2 \qquad \Delta_rH^o = -1.6184(4) \text{ eV} \qquad (3)$$

$$IO^+ + e^- \rightarrow I + O \qquad \Delta_rH^o = -7.37 \pm 0.02 \text{ eV} \qquad (4)$$

where 0 K thermicities are derived from the Active Thermochemical Tables.[17] Reaction 1 was assumed to occur at 4.5 $\times 10^{-10}$ cm^3 s^{-1}, two-thirds the Langevin capture rate constant.[18] Reactions 2 and 3 were assumed to occur at the Langevin capture values, 5.5 $\times 10^{-10}$ cm^3 s^{-1} and 1.07 $\times 10^{-9}$ cm^3 s^{-1}, respectively, with reaction 2 proceeding entirely through channel 2a. Reaction 4, the dissociative recombination of IO^+, was assumed to have the same rate constant as the dissociative recombination of O_2^+, 2×10^{-7} cm^3 s^{-1} at room temperature.

Here, we provide experimental determinations of the relevant I^+ and IO^+ chemistries with O, O_2, and O_3 between 150 – 300 K, covering most of the atmospherically relevant temperature range. The charge exchange reaction 3 with neutral iodine atoms and the dissociative recombination of IO^+ reaction 4 are not addressed. The updated rate constants are incorporated into the prior WACCM-X model and the impacts discussed.

Methods

Experimental

Kinetics were measured using the previously described variable-ion source temperature-adjustable selected-ion flow tube (VISTA-SIFT) shown in Figure 1.[12] Briefly, reactant ions (either I^+ or IO^+) were produced in a flowing afterglow source.[12] Helium (99.999% Matheson) was discharged inside a 1" diameter glass tube passing through an Evenson-style cavity[19] operated at 30 W and 2.6 GHz. Resulting He^+, He_2^+, and metastable He^* entered a 5-cm diameter stainless steel flow tube operated at ~ 1 Torr and reacted with CF_3I introduced through a precision needle valve (Granville Phillips). Multiple species were produced, including I^+. The concentration of CF_3I, while not explicitly determined, was kept small (<10^{11} cm^{-3}) to minimize the secondary reaction of I^+ with CF_3I.[12] Quenching of excited states of I^+ by the helium buffer gas is inefficient and an additional quenchant (N_2O ~100 std. cm^3 min^{-1}) was added downstream. The presence of excited states of I^+ was monitored by reaction with Cl_2.[14] A single-exponential decline in the I^+ signal, consistent with the literature rate constant (k = 4.5 × 10^{-11} cm^3 s^{-1}), indicated that the reaction was dominated by the ground-state $^3P_2$ channel. Excited state reactants (either the triplet spin-orbit states or the singlet electronic state) may remain present at <5% of total ions. IO^+ was produced by oxidation of I^+ by O_3 in the flowing afterglow source; a mixture of O_2 and O_3 was introduced using an O_3 generator.

Ions were transported through a series of rectilinear quadrupole ion guides[20] and quadrupole benders (the benders couple to alternative ion sources not used in the present study) to a quadrupole mass filter. The desired reactant ion was mass-selected and transported to the reactant flow tube using a series of trapezoidal ion guides to compress the radial extent of the ion packet and a Venturi inlet to inject the ions into a large helium flow (typically 14 std. L min^{-1}) entering the reaction flow tube.

Neutral reactants were introduced either 59 cm (O_2, O_3) prior to the terminus of the 1-m long, 7.3 cm diameter stainless steel flow tube through 1/8" diameter finger inlets or 49 cm (O) from the terminus though a ½" pyrex tube, surrounded by stainless steel shim to prevent charging. The pressure of the flow tube was monitored using a capacitance manometer through a port 29.5 cm prior to the terminus. Typical flow tube pressure was 0.35 Torr. The temperature of the flow tube was varied from room temperature to 150 K by flowing liquid nitrogen through three zones of copper coils surrounding the flow tube plus precooling the helium. The temperature of each zone was actively monitored using an resistive temperature device (RTD) and the liquid nitrogen flow metered using solenoid valves actuated by proportional-integral-derivative (PID) temperature controllers (Omega).

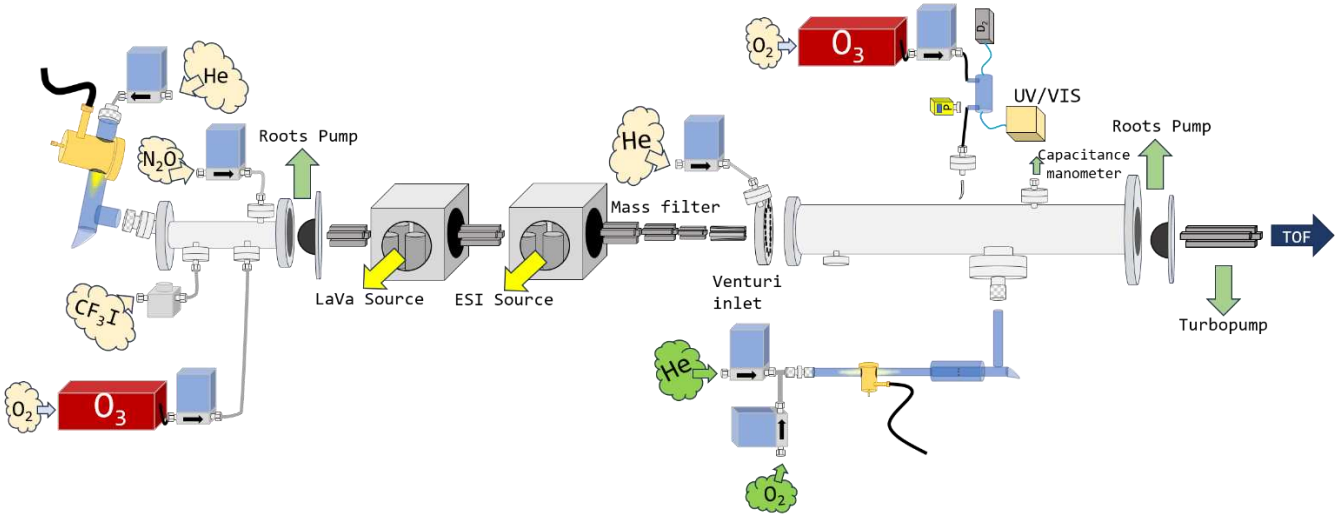

Figure 1. Cartoon schematic of the VISTA-SIFT apparatus as used in the present experiment.

Ions were sampled through a 2-mm aperture in a rounded molybdenum nose cone and transported to a high vacuum region using a rectilinear quadrupole ion guide. Ions entered an orthogonally-accelerated Reflectron time-of-flight mass spectrometer (Jordan TOF, Inc.) pulsed at 10 kHz and were detected using a "Z-stack" of three microchannel plates and counted by a time to digital converter (Fast ComTec).

Kinetics with the three oxygen allotropes were measured in separate experiments by monitoring reactant and product ions as a function of neutral concentration. O_2 (99.999%, Matheson) reactant was used neat and metered using a mass flow controller.

O_3 was produced using a commercial generator (Absolute Ozone, Atlas). O_2 (99.98% Matheson) was partially converted to O_3 and metered using a mass flow controller (MKS Inst.) into a 10-cm long absorption cell. The transmission of light from a deuterium lamp source (OtO photonics LS-DH) through the cell was monitored using a UV/VIS spectrometer (Ocean Optics, STS-UV). The O_3 concentration was determined from the absorption at 298 nm, the total mass flow rate, and the pressure in the absorption cell.[21] Typical O_3 concentrations were 16% of the nominal O_2 flow.

$O(^3P)$ was produced by microwave discharge of dynamically-mixed helium and between 0 – 4% O_2.[22] The $O(^3P)$ concentration was quantified by VUV absorption spectroscopy using the multiplet near 130 nm. About 10% of O_2 were dissociated at smaller O_2 flows, decreasing to about 8% at higher O_2 flows. Charge transfer and oxygen abstraction reactions of I^+ and IO^+ with O_2 and $O_2(^1\Delta_g)$ are endothermic and cannot occur under thermal conditions. An alternative method of producing $O(^3P)$ by titration of N with NO was disfavored due to the complication of competing reactions of IO^+ with N and NO. In separate experiments, the rate constants derived using these two methods have been consistent; further details are given in supporting information.

Quantum Chemical Calculations

Density functional calculations were performed at the B3LYP/def2-TZVP level[23] using the Gaussian 16 quantum chemical package.[24] Minima and transition states were confirmed to contain either zero or one imaginary frequency under normal mode analysis. Intrinsic reaction coordinate calculations were performed on each transition state to confirm the connecting minima. Where energies are reported, they are zero-point corrected. All species were calculated unrestricted at singlet, triplet, and quintet multiplicities.

Kinetic Analysis

Kinetic data was analyzed using the Statistical Kinetic Analysis (SKA) method. The reaction system is represented as a system of ordinary differential equations (ODEs) and numerically integrated using a Dormand-Prince 5(4) solver for a given set of rate constants and the initial concentrations of each species. By repeatedly integrating this set of ODEs to the reaction time, and for each of the neutral concentrations, a simulated matrix of each species is produced for our reaction conditions. This simulated matrix is compared the measured matrix to calculate a goodness-of-fit (GOF) value that quantifies how similar the matrices are. A best fit is found by varying the rate constants to minimize the GOF using the JADE implementation of the differential evolution algorithm, and the rate constants are recorded.

Error is analyzed by bootstrapping. The measured data is resampled, with replacement, to produce a trial set of data. This trial is then refit using the same method as above, and the best fit rate constants are recorded. This process is repeated 500 times to build up a distribution of best fit rate constants, with the error in each rate constant represented by the total width of its specific distribution.

Results

Quantum chemical calculations

Calculated reaction coordinates for the indicated reactions are shown in Figures 2 - 5. In addition to reactions 1-4, this includes

$$IO^+ + O_3 \rightarrow IO_2^+ + O_2 \qquad \Delta_rH^o = -3.0 \text{ eV} \qquad (5a)$$

$$\rightarrow I^+ + 2O_2 \qquad \Delta_rH^o = -1.0 \text{ eV} \qquad (5b)$$

where the thermicities are calculated at the B3LYP/def2-TZVP level. Spin-orbit coupling is not considered in the calculations although it is certainly significant in these systems.

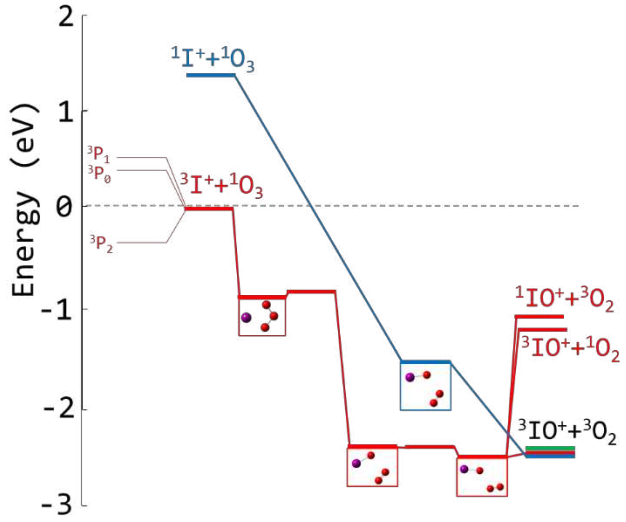

Figure 2. Reaction coordinate for $I^+ + O_3$ calculated at the B3LYP/def2-TZVP level. The multiplicity of each coordinate [triplet (red), singlet (blue)] is indicated. A quintet state of $IO^+(O_2)$ is omitted for clarity. Leading superscripts indicate the multiplicities of separated species. Iodine atoms are shown in purple, oxygen atoms are shown in red.

Some general chemical intuition concerning these systems is gained by noting that I^+ is valence isoelectronic with O, IO^+ with O_2, and IO_2^+ with O_3. I^+, like O, has a $^3P_2$ ground state, but with much larger spin-orbit splitting between the J = 0 and 1 states. Calculated IO^+ and IO_2^+ structures are shown in Figure 3. IO^+ has a triplet ground state with a singlet excited state, like

O_2, but with a larger splitting of 1 eV. IO^+ has a significantly smaller bond dissociation energy (3.05 eV) than O_2 (5.11 eV). IO_2^+ can form an analogue to O_3, a triplet C_{2V} structure, calculated to be slightly (0.2 eV) higher in energy than the electrostatically bound triplet $I^+(O_2)$ isomer. The $I^+(O_2)$ structure is weakly bound (0.2 eV) to O_2 dissociation, while the O_3 analogue is more strongly bound due to a > 1 eV barrier that must be overcome to dissociate. The OI^+-O BDE is calculated to be 2.0 eV, larger than that of O_2-O, 1.1 eV. The interplay of IO_2^+ structures is illustrated in Figure 4.

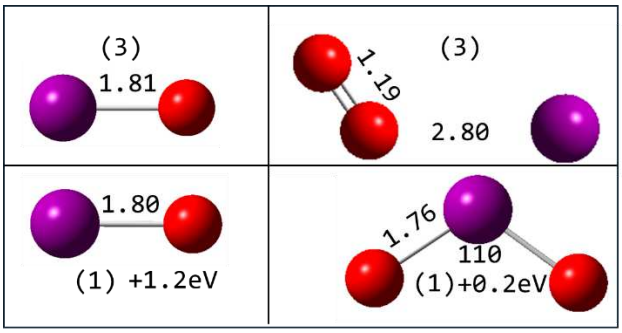

Figure 3. Structures of IO^+ and IO_2^+ calculated at the B3LYP/def2-TZVP level. Bond distances (Å), bond angles (degrees), multiplicities (in parentheses), and energies relative to the triplet ground states are indicated. Iodine atoms are shown in purple, oxygen atoms are shown in red.

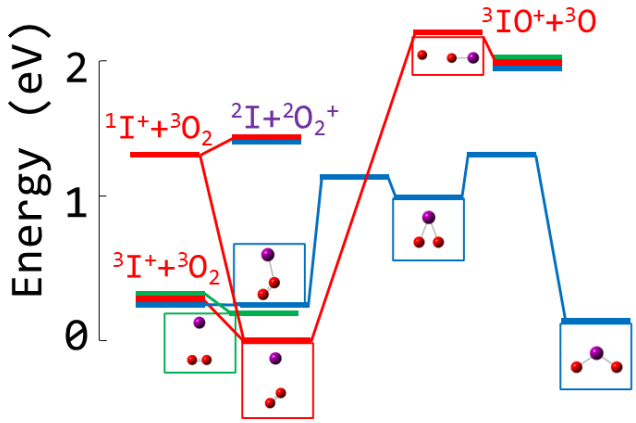

Figure 4. A portion of the $[IO_2]^+$ system calculated at the B3LYP/def2-TZVP level with singlet (blue), triplet (red), and quintet (green) multiplicities. Leading superscripts indicate the multiplicities of separated species. Iodine atoms are shown in purple, oxygen atoms are shown in red.

Reaction 1, $I^+ + O_3$, (Figure 2) is calculated to be barrierless. It is exothermic to produce either excited state singlet O_2 or singlet IO^+. Reaction 2, $IO^+ + O$, (Figure 5) can proceed on singlet,

triplet, or quintet reaction surfaces. The triplet and quintet pathways are calculated to have small energetic barriers, while the singlet pathway is fully submerged. Crossing points between surfaces were not explicitly calculated but given the large spin-orbit coupling expected for heavy atoms, intersystem crossing is likely to be efficient.

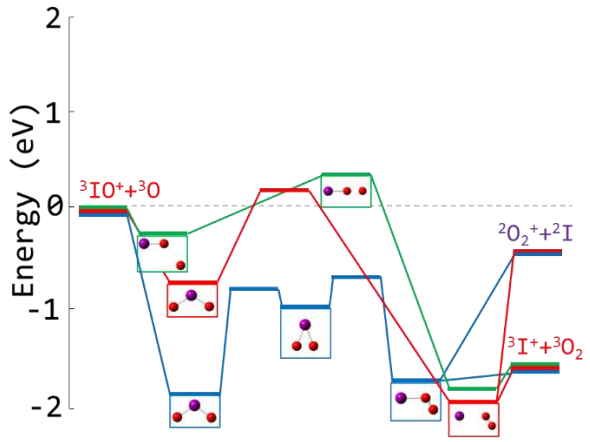

Figure 5. Reaction coordinate for $IO^+ + O$ calculated at the B3LYP/def2-TZVP level. The multiplicity of each coordinate (singlet (blue), triplet (red), quintet (green)) is indicated. Leading superscripts indicate the multiplicities of separated species. Iodine atoms are shown in purple, oxygen atoms are shown in red.

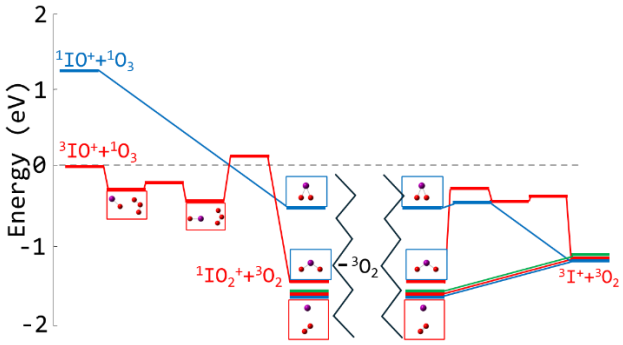

Figure 6. Reaction coordinate for $IO^+ + O_3$ calculated at the B3LYP/def2-TZVP level. The break indicates the loss of an initial O_2; to the right of the break the possible sequential loss of a second O_2 . The multiplicity of each coordinate (triplet (red), singlet (blue), and quintet (green)) is indicated. Leading superscripts indicate the multiplicities of separated species. Iodine atoms are shown in purple, oxygen atoms are shown in red.

Reaction 5, $IO^+ + O_3$, (Figure 6) is exothermic both to oxidation of IO^+ to IO_2^+ and the "apparent reduction" of IO^+ to I^+. Although reaction 5b could appear to reflect I^+ oxidation of O_3, it is better understood as a harsh oxidation of IO^+ by O_3 that leaves the IO_2^+ product with enough internal energy for further dissociation. To proceed on the triplet surface of the initial oxidation, the reaction must overcome a small energetic barrier

Kinetics

Bimolecular reactions of I^+ and IO^+ with O_2 are highly endothermic and cannot occur under thermal conditions. Association of I^+ with O_2 is bound by 0.2 eV as calculated at CAM-B3LYP/def2-TZVP. The calculated equilibrium constant reaches K^o=~1 at 150 K. Statistical calculations indicate a small rate constant of less than 10^{-29} cm^6 s^{-1} at that temperature, negligible in the upper atmosphere. Note that any association would be expected to form triplet $I^+(O_2)$ as the O_3 analogue singlet OIO^+ is calculated 0.2 eV higher in energy and would require a substantial barrier to rearrangement. IO_3^+ similarly is calculated to be a weakly bound (0.2 eV) cluster and the association to $IO^+(O_2)$ may be stable at below ~150 K. Empirically, I^+ and IO^+ are, as expected, inert to O_2 under the experimental conditions here with rate constants <10^{-12} cm^3 s^{-1}.

$$I^+ + O_2 \rightarrow IO^+ + O \qquad \Delta_rH^o = 2.05 \pm 0.02 \text{ eV} \qquad (6a)$$

$$\rightarrow I^+(O_2) \qquad \Delta_rH^o = -0.2 \text{ eV } K_{200} = 0.07 \qquad (6b)$$

$$IO^+ + O_2 \rightarrow IO_2^+ + O \qquad \Delta_rH^o = 3 \text{ eV} \qquad (7a)$$

$$\rightarrow IO^+(O_2) \qquad \Delta_rH^o = -0.2 \text{ eV } K_{200} = 0.4 \qquad (7b)$$

Thermicities with uncertainties indicated are derived from literature values where available,[17] and from calculations at the B3LYP/def2-TZVP level where not. This fact simplifies the experimental measurements of reaction with O and O_3, obviating the need to produce those species without O_2 present or to deconvolute the reactivity.

Typical measured ion counts of reactant IO^+ as a function of $O(^3P)$ concentration are shown in Figure 7. A single exponential decay of IO^+ was observed. Reaction 2b, production of O_2^+, was not observed, setting an upper limit of 10^{-12} cm^3 s^{-1}. Derived rate constants and uncertainty distributions for reaction 2a as a function of temperature are shown in Figure 8.

The rate constants k_{2a} is well-represented across this temperature range by $1.6 \pm 0.5 \times 10^{-10}$ cm^3 s^{-1} (T / 200 K)$^{-2}$. The Langevin capture rate k_L is 5.5×10^{-10} cm^3 s^{-1}, and somewhat larger ($k_{cap} = k_L + 1.1\times10^{-10}$ cm^3 s^{-1} (T / 200 K)$^{0.35}$) if attraction due to higher order electric moments of IO^+ are considered.[25,26] Extrapolation of the power law fit will exceed k_{cap} and become unphysical at temperatures below 100 K.

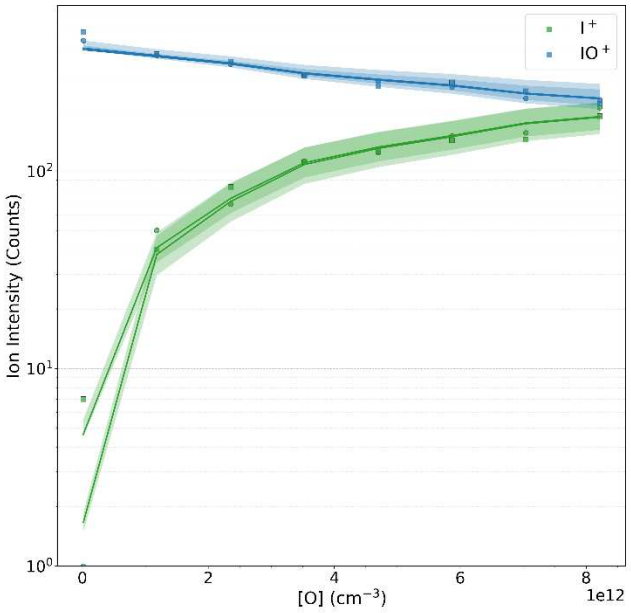

Figure 7. . Example measured counts of IO^+ and I^+ as a function of O atom concentration at 250 K. Multiple data sets are simultaneously fit, shown by different shades of blue (IO^+) and green (I^+). The dark lines indicate the median fit, with shaded regions showing the uncertainty.

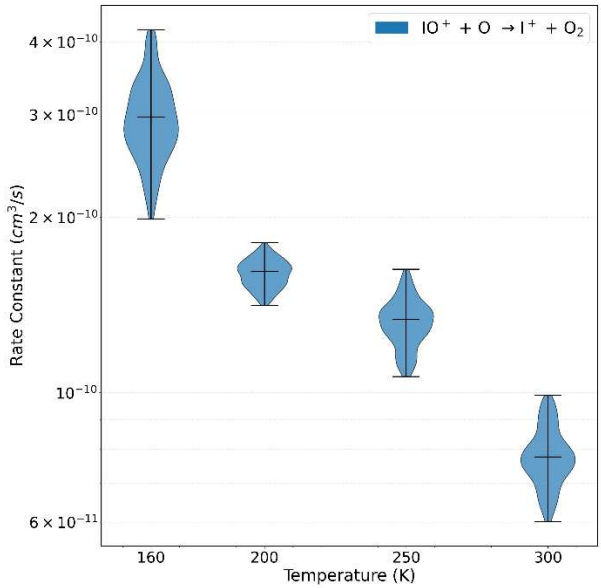

Figure 8. $IO^+ + O \rightarrow I^+$ rate constant as a function of temperature. Rate constants are shown as violin plots, where the widest part is the most probable value. Taller violins represent less well

defined rate constants than shorter ones. The most probable, and extreme points, as shown by solid horizontal lines. The uncertainty in a rate constant is taken by the total spread of the distribution.

Typical measured counts of I^+ and products as a function of O_3 concentration are shown in Figure 9.

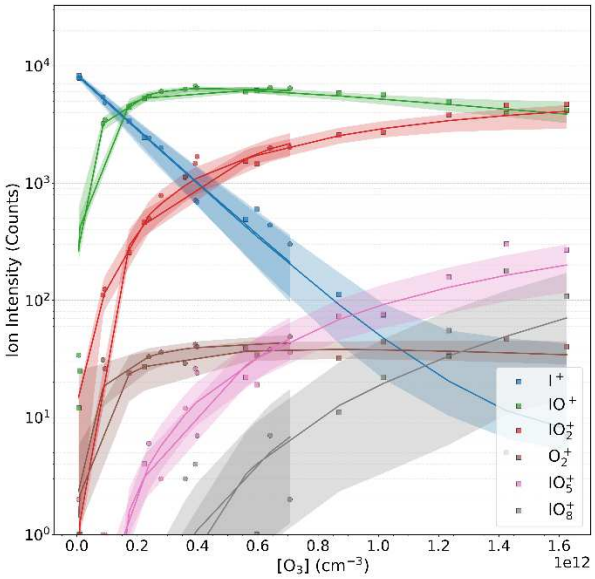

Figure 9. Measured ion counts for $I^+ + O_3 \rightarrow IO^+ + O_2$ and subsequent reactions as a function of O_3 concentration. Multiple data sets are fit simultaneously, indicated by different shades of blue (I^+), green (IO^+), red (IO_2^+), brown (O_2^+), pink (IO_5^+), and gray (IO_8^+). The dark lines indicate the median fit, with the shaded regions indicating the uncertainty.

Derived rate constants and uncertainty distributions for reactions 1 ($I^+ + O_3$) and 5 ($IO^+ + O_3$) as a function of temperature are shown in Figure 10.

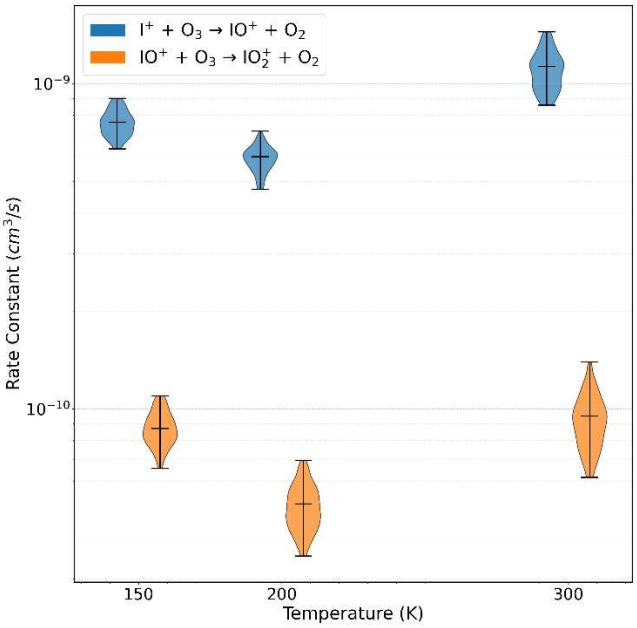

Figure 10. Rate constants for the reactions $I^+ + O_3 \rightarrow IO^+ + O_2$ (blue) and $IO^+ + O_3 \rightarrow I^+ + 2O_2$ (green) as a function of temperature. Rate constants are shown as violin plots, where the widest part is the most probable value. Taller violins represent less well-defined rate constants than shorter ones. The most probable, and extreme points, as shown by solid horizontal lines. The uncertainty in a rate constant is taken by the total spread of the distribution.

Reaction 1 ($I^+ + O_3$) proceeds near the capture rate constant[27] (8.9×10^{-10} cm^3 s^{-1} $(T/200K)^{-0.15}$ with the temperature dependence due to the dipole moment of O_3 (contributions from higher order terms are negligible). The apparent dip at 200 K is most likely an artifact of the experiment or of the analysis, but not one we were able to identify. We recommend the capture rate constant for reaction 1 at all temperatures.

Reaction 5a, $IO^+ + O_3 \rightarrow IO_2^+ + O_2$ proceeds with an average rate constant of about 8×10^{-11} cm^3 s^{-1}. The 200 K point may be spuriously low. The reaction occurs well below the capture rate constant (8.7×10^{-10} cm^3 s^{-1} $(T/200K)^{-0.15}$) with a possible large hard sphere component increasing the value by ~20% at 300 K). The slight dip in the temperature dependence makes extrapolation outside the temperature range difficult. We recommend $8\pm2\times10^{-11}$ cm^3 s^{-1} across the temperature range. The product here must be the O_3 analogue, singlet OIO^+, which is metastable but significantly more bound than the lower energy $I^+(O_2)$ isomers.

Reaction 5b, the harsh oxidation reforming I^+, occurs inefficiently, if at all. The reaction would present itself as "curvature" in the primary I^+ decay. Such curvature is absent for the first two orders of magnitude decrease in the I^+ signal and possible (but not clearly present) only in the

third order of magnitude decrease. The data provide an upper limit of 10^{-11} cm^3 s^{-1} on reaction 5b.

Despite being significantly exothermic, we see no definitive evidence of the bimolecular reaction 8a of IO_2^+ with O_3. Instead, the association reaction 8b

$$IO_2^+ + O_3 \rightarrow IO^+ + 2O_2 \qquad \Delta_rH^o = -1.8 \text{ eV} \qquad (8a)$$

$$IO_2^+ + O_3 + He \rightarrow IO_5^+ + He \qquad (8b)$$

is observed occurring close to the capture rate, along with further clustering with O_3 to yield IO_8^+ and IO_{11}^+ at the lowest temperature. At most, ~10% of reaction 8 occurs through 8a under the present conditions.

Table I. Recommended rate constants for $IO_x^+ + O_y$ reactions

Reaction	k (cm^3 s^{-1})
$I^+ + O_2$	$<10^{-12}$
$IO^+ + O_2$	$<10^{-12}$
$IO^+ + O \rightarrow I^+ + O_2$	$1.6 \pm 0.5 \times 10^{-10} (\frac{T}{200\ K})^{-2}$ | T > 100 K $5.5\times10^{-10} + 1.1\times10^{-10}$ (T / 200 K)$^{0.35}$ | T<100 K
$I^+ + O_3 \rightarrow IO^+ + O_2$	$8.9 \pm 1 \times 10^{-10} (\frac{T}{200\ K})^{-0.15}$
$IO^+ + O_3 \rightarrow IO_2^+ + O_3$	$8 \pm 2 \times 10^{-11}$
$IO_2^+ + O_3 \rightarrow IO^+ + 2O_2$	$< 5 \times 10^{-11}$

Atmospheric Implications

The measured rate constants were input into the global 3-D Whole Atmosphere Community Climate Model (WACCM), which extends vertically from the surface up to the lower thermosphere (~140 km).[9,28] As in our previous study of the impact of thermospheric iodine emissions on the stratosphere,[9] we employed for the present study WACCM version 4 (WACCM4), which uses the NCAR community Earth System Model (CESM version 1.1.1) as a common numerical framework.[29] WACCM4 is a comprehensive numerical model with detailed descriptions of processes throughout the atmosphere (e.g., Marsh et al.[30]), which has been widely used for the Coupled Model Intercomparison Project (e.g., Eyring et al. [31]), Chemistry-Climate Model Initiative (CCMI) (e.g., Morgenstern et al.,[32] Orbe et al.[33]), and other detailed process studies. The horizontal resolution is 1.95° latitude x 2.5 ° longitude, with 88 vertical levels from the surface to 5.96 $\times10^{-6}$ hPa, providing a vertical resolution of ~1.2 km in the troposphere/lower stratosphere and ~3.5 km in the mesosphere/lower thermosphere.

For neutral iodine chemistry we used the detailed chemistry scheme from Cuevas et al. (2022),[34] supplemented by reactions of HOI and HI with O and H atoms, where the rate constants are

estimated by quantum theory calculations and transition state theory.[9] For the ion-molecule chemistry of iodine, I^+ forms from charge transfer between I and O_2^+, and neutralization through dissociative recombination of IO^+ with electrons.[9] In the previous study, reaction 1 ($I^+ + O_3$) was assigned a rate constant of 4.5×10^{-10} cm^3 s^{-1} independent of temperature; this estimate is ~66% of the simple Langevin capture rate constant, which accounts for the branching ratio into the $^3IO^+$ ground state (Figure 2). However, the present study shows that the reaction rate is significantly enhanced by the O_3 dipole moment. Assuming that $^1IO^+$ is rapidly quenched to $^3IO^+$ by collisions with air molecules, or reacts at a similar rate as $^3IO^+$ with O and electrons, we now adopt the measured k_1 in WACCM i.e. a rate which is ~2 times faster at 200 K. For reaction 2a ($IO^+ + O$), the measured rate constant at 200 K is 3.4 times slower than the Langevin limit used in Feng et al. (2023), and this discrepancy will increase in the warmer lower thermosphere. Of the other reactions in Table 1, reaction 5a oxidizes IO^+ to IO_2^+. IO_2^+ very likely reacts with O to form $IO^+ + O_2$. The rate constant for this reaction was set to that for reaction 2a, and the rate constant for dissociative electron recombination of IO_2^+ was set to the (typical) value of 2×10^{-7} cm^3 s^{-1} used for dissociative recombination of IO^+.

In order to observe the changes in iodine chemistry in the middle and upper atmosphere that result from the present study, two simulations of 1 year duration were performed. The control run used the base case scenario of thermospheric injection of I^+ from small satellites (TII1) and original iodine chemistry in Feng et al. (2023). The second run used the modified ion-molecule chemistry from the present study. The specified-dynamics (SD) version of WACCM (SD-WACCM), which is nudged to the MERRA-2 reanalysis dataset,[35] was used to ensure that both model simulations had the same winds and temperatures below 50 km.[36] Both simulations used the same initialization conditions file produced after running for 15 years up to 2013.[9] The model was then run for the whole of year 2014 (this is because the observed external forcings used from CMIP6[31] are only available up to early 2015).

Figure 11 shows the vertical profiles (globally averaged) of I^+ and I, for the base case run[9] and with the new rate constants and chemistry from the present study. As expected, given the increase in k_1 and decrease in k_{5a} in the new chemistry, there is an increased rate of neutralization of I^+, so I increases and I^+ decreases (cf. the red and black curves in Figure 11(a)). The lower panel (b) shows the fractional change in I, which starts to increase from zero below 110 km, where O_3 present at sufficient concentrations for reaction 4 to come into play. The largest fractional increase (a factor of 1.8) occurs just above 80 km. The fractional change returns to zero below 60 km because the I concentration is several orders of magnitude larger than I^+, as shown in Figure 11(a). The fractional change in I^+ is zero above 110 km (where there is very little O_3) and then becomes increasingly negative at lower altitudes.

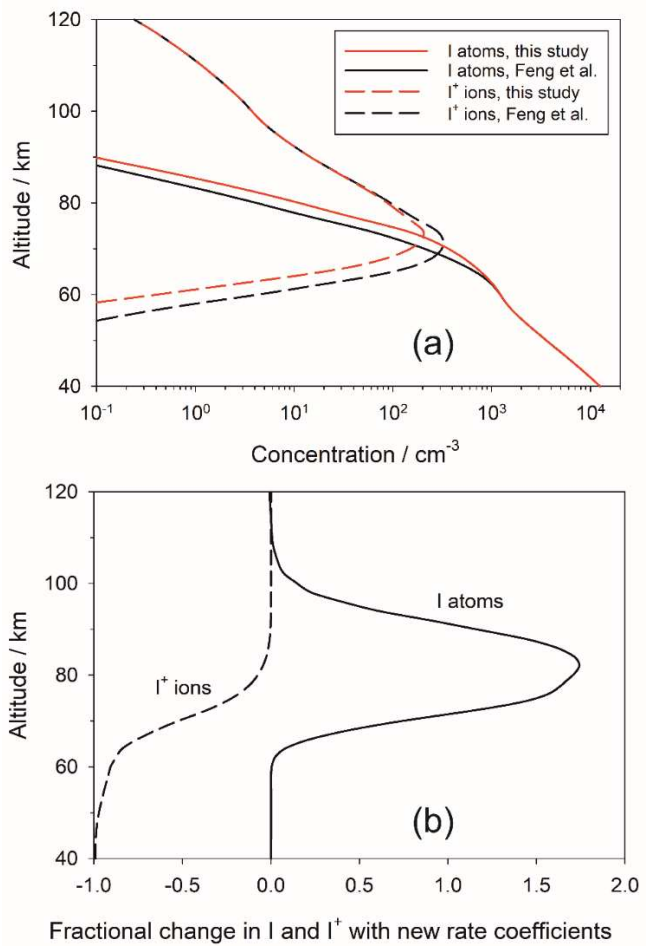

Figure 11. (a) Vertical profiles (globally averaged) of the I^+ and I concentrations, for the base case run[9] and with the new chemistry and rate constants from the present study; (b) the fractional change in I^+ and I as a function of altitude.

A more detailed picture is provided by the diurnal variations in the vertical profiles of I^+, I and their ratio, shown in Figure 12. These are annual averages, at the equator. The top row shows the results from Feng et al. (2023), and the bottom row the results from the present study. Note that the large increase in I (panels (a) and (d)) during daytime below 60 km results from the photolysis of various neutral iodine-containing reservoir species (HOI, INO_3 etc.). In this region of the atmosphere ion-molecule chemistry is not significant, so the two models are essentially identical. With the new chemistry there is an increase in I between 60 and 100 km (panels (a) and (d)) accompanied by a marked decrease in I^+ (panels (b) and (e)). Comparing the I^+/I ratio plots in panels (c) and (f) illustrates the balance shifting to I between 60 and 100 km with the new chemistry.

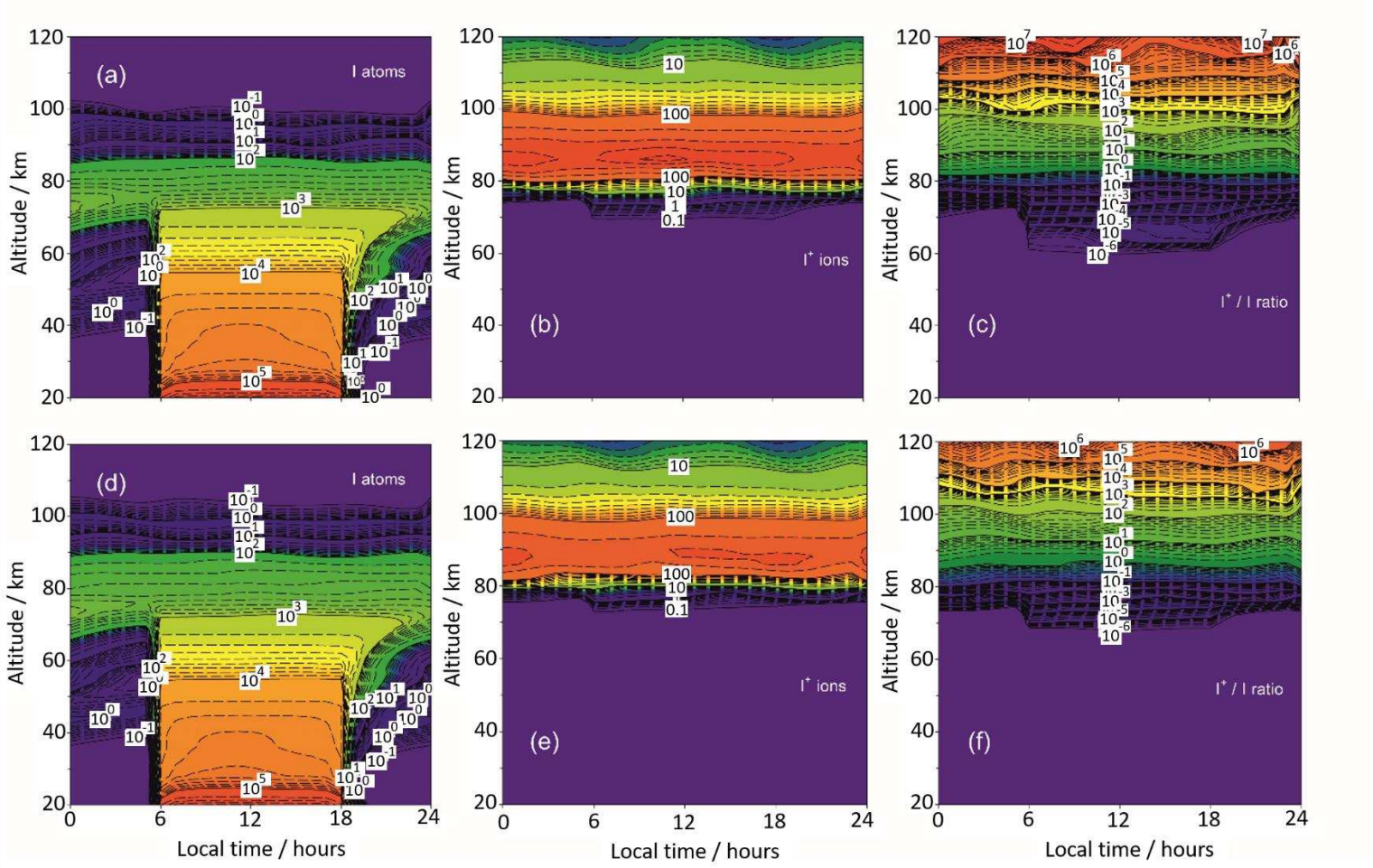

Figure 12. Diurnal variations in the vertical profiles of I^+, I and the I^+/I ratio at the equator: top row shows the results from Feng et al. (2023),[9] and the bottom row the model results with the new chemistry and rate constants.

Conclusions

The kinetics of ion-molecule chemistry of IO_n^+ (n = 0 – 2) with O, O_2, and O_3, of upper atmospheric interest, were measured over the temperature range 160 – 300 K. The rate constants for these reactions had previously been estimated and implemented in WACCM to determine the impact of iodine released from small satellite propulsion systems. The model was updated using the rate constants reported here. Above 100 km the changes to the I and I^+ abundances from those previously reported[9] are negligible. The predicted I abundance is increased by a factor of 1.7 between 80 – 85 km and unchanged at altitudes below 60 km. The predicted I^+ abundance is decreased at altitudes below 80 km.

Online Supporting Information

- Details of $O(^3P)$ production and characterization
- Calculated structures and energies

Acknowledgements

This work is supported by the Air Force Office of Scientific Research under AFOSR-25RVCOR006.

The views expressed are those of the authors and do not reflect the official guidance or position of the Department of the Air Force, the Department of Defense (DoD), or the U.S. government. The appearance of external hyperlinks does not constitute endorsement by the United States DoD of the linked websites, or the information, products, or services contained therein. The DoD does not exercise any editorial, security, or other control over the information you may find at these locations.

References

(1) Kellogg, W. W. Pollution of the Upper Atmosphere by Rockets. *Space Sci. Rev.* **1964**, 275–316.

(2) Prather, M. J.; García, M. M.; Douglass, A. R.; Jackman, C. H.; Ko, M. K. W.; Sze, N. D. The Space Shuttle's Impact on the Stratosphere. *J. Geophys. Res. Atmos.* **1990**, *95*, 18583–18590. https://doi.org/https://doi.org/10.1029/JD095iD11p18583.

(3) Sharma, S. P. *Impact of Spaceflight on Earth's Atmosphere: Climate, Ozone, and the Upper Atmosphere*; 2024.

(4) Sirieys, E.; Gentgen, C.; Jain, A.; Minton, J.; Weck, O. L. de. Space Sustainability Isn't Just about Space Debris: On the Atmospheric Impact of Space Launches. *MIT Sci. Policy Rev.* **2022**, *3*, 143–151. https://doi.org/doi.org/10.38105/spr.whfig18hta.

(5) Brown, T. F. M.; Bannister, M. T.; Revell, L. E. Envisioning a Sustainable Future for Space Launches: A Review of Current Research and Policy. *J. R. Soc. New Zeal.* **2024**, *54*, 273–289. https://doi.org/https://doi.org/10.1080/03036758.2022.2152467.

(6) Ryan, R. G.; Marais, E. A.; Balhatchet, C. J.; Eastham, S. D. Impact of Rocket Launch and Space Debris Air Pollutant Emissions on Stratospheric Ozone and Global Climate. *Earth's Futur.* **2022**, *10*, e2021EF002612. https://doi.org/https://doi.org/10.1029/2021EF002612.

(7) Rafalskyi, D.; Martínez, J. M.; Habl, L.; Rossi, E. Z.; Proynov, P.; Boré, A.; Baret, T.; Poyet, A.; Lafleur, T.; Dudin, S.; Aanesland, A. In-Orbit Demonstration of an Iodine Electric Propulsion System. *Nature* **2021**, *599*, 411–415.

(8) Bianchi, F. M.; Vinci, A. E.; Garrigues, L. Global Modeling of Iodine Hall Thruster Performance and Discharge Properties. *J. Appl. Phys.* **2025**, *137*, 43301. https://doi.org/10.1063/5.0244131.

(9) Feng, W.; Plane, J. M. C.; Chipperfield, M. P.; Saiz-Lopez, A.; Booth, J.-P. Potential Stratospheric Ozone Depletion Due To Iodine Injection From Small Satellites. *Geophys. Res. Lett.* **2023**, *50*, e2022GL102300.

(10) Liu, H.-L.; Bardeen, C. G.; Foster, B. T.; Lauritzen, P.; Liu, J.; Lu, G.; Marsh, D. R.; Maute, A.; McInerney, J. M.; Pedatella, N. M.; Qian, L.; Richmond, A. D.; Roble, R. G.; Solomon, S. C.; Vitt, F. M.; Wang, W. Development and Validation of the Whole Atmosphere Community Climate Model With Thermosphere and Ionosphere Extension (WACCM-X 2.0). *J. Adv. Model. Earth Syst.* **2018**, *10*, 381–402. https://doi.org/https://doi.org/10.1002/2017MS001232.

(11) Pottie, R. F.; Barker, R.; Hamill, W. H. Ion-Molecule Reactions of Methyl and Ethyl Iodides. *Radiat. Res.* **1959**, *10*, 664–670. https://doi.org/10.2307/3570650.

(12) Morris, R. A.; Van Doren, J. M.; Viggiano, A. A.; Paulson, J. F. Reactions of Ar^+ with Halocarbons and of I^+ with CF_3I. *J. Chem. Phys.* **1992**, *97*, 173–179. https://doi.org/10.1063/1.463605.

(13) Edmonds, P. H.; Hasted, J. B. A Near-Resonance Charge Transfer Process. *Proc. Phys. Soc.* **1964**, *84*, 99. https://doi.org/10.1088/0370-1328/84/1/314.

(14) Spanel, P.; Tichy, M.; Smith, D. The Reactions of Positive and Negative Halogen Ions with Cl_2 and Br_2. *J. Chem. Phys.* **1993**, *98*, 8660–8666.

(15) van de Guchte, W. J.; van der Hart, W. J.; de Koning, L. J.; Nibbering, N. M. M.; Dunbar, R. C. Formation of Long-Lived Benzene Ions during Charge Exchange Ionization of 1,5-Hexadiyne in an Ion Cyclotron Resonance Spectrometer. *Int. J. Mass Spectrom. Ion Process.* **1993**, *123*, 11–17. https://doi.org/https://doi.org/10.1016/0168-1176(93)87049-X.

(16) Koyanagi, G. K.; Bohme, D. K. Kinetics and Thermodynamics for the Bonding of Benzene to 20 Main-Group Atomic Cations: Formation of Half-Sandwiches, Full-Sandwiches and Beyond. *Int. J. Mass Spectrom.* **2003**, *227*, 563–575. https://doi.org/https://doi.org/10.1016/S1387-3806(03)00091-5.

(17) Ruscic, B.; Bross, D. H. *Active Thermochemical Tables (ATcT) based on ver. 1.130 of the Thermochemical Network (2026); available at ATcT.anl.gov*. https://atct.anl.gov.

(18) Tsikritea, A.; Diprose, J. A.; Softley, T. P.; Heazlewood, B. R. Capture Theory Models: An Overview of Their Development, Experimental Verification, and Applications to Ion–Molecule Reactions. *J. Chem. Phys.* **2022**, *157*, 60901. https://doi.org/10.1063/5.0098552.

(19) Fehsenfeld, F. C.; Evenson, K. M.; Broida, H. P. Microwave Discharge Cavities Operating at 2450 MHz. *Rev. Sci. Instrum.* **1965**, *36*, 294–298. https://doi.org/10.1063/1.1719557.

(20) Taormina, C. R.; Nicolette, E.; Novak, T.; Pedder, R. E. An Ion Guide Study: Quadrupoles, Rectinlinear Quadrupoles, Hexapoles, and Octopoles. *56th Meet. Am. Soc. Mass Spectrom.* **2008**, https://ardaratech.com/downloads/technical-notes/1.

(21) Williams, S.; Knighton, W. B.; Midey, A. J.; Viggiano, A. A.; Irle, S.; Wang, Q. F.; Morokuma, K. Oxidation of Alkyl Ions, $C_nH_{2n+1}^+$ (N=1-5), in Reactions with O_2 and O_3 in the Gas Phase. *J. Phys. Chem. A* **2004**, *108*, 1980–1989. https://doi.org/10.1021/jp031099+.

(22) Shuman, N. S.; Miller, T. M.; Ard, S. G.; Viggiano, A. A. The Associative Ionization of N(2P) + O(3P). *J. Chem. Phys.* **2024**, *160*, 114309. https://doi.org/10.1063/5.0188483.

(23) Weigend, F.; Ahlrichs, R. Balanced Basis Sets of Split Valence, Triple Zeta Valence and Quadruple Zeta Valence Quality for H to Rn: Design and Assessment of Accuracy. *Phys. Chem. Chem. Phys* **2005**, *7*, 3297.

(24) Frisch, M. J.; Trucks, G. W.; Schlegel, H. B.; Scuseria, G. E.; Robb, M. A.; Cheeseman, J. R.; Scalmani, G.; Barone, V.; Petersson, G. A.; Nakatsuji, H.; Li, X.; Caricato, M.; Marenich, A. V; Bloino, J.; Janesko, B. G.; Gomperts, R.; Mennucci, B.; Hratchian, H. P.; Ortiz, J. V; Izmaylov, A. F.; Sonnenberg, J. L.; Williams-Young, D.; Ding, F.; Lipparini, F.; Egidi, F.; Goings, J.; Peng, B.; Petrone, A.; Henderson, T.; Ranasinghe, D.; Zakrzewski, V. G.; Gao, J.; Rega, N.; Zheng, G.; Liang, W.; Hada, M.; Ehara, M.; Toyota, K.; Fukuda, R.; Hasegawa, J.; Ishida, M.; Nakajima, T.; Honda, Y.; Kitao, O.; Nakai, H.; Vreven, T.; Throssell, K.; Montgomery Jr., J. A.; Peralta, J. E.; Ogliaro, F.; Bearpark, M. J.; Heyd, J. J.; Brothers, E. N.; Kudin, K. N.; Staroverov, V. N.; Keith, T. A.; Kobayashi, R.; Normand, J.; Raghavachari, K.; Rendell, A. P.; Burant, J. C.; Iyengar, S. S.; Tomasi, J.; Cossi, M.; Millam, J. M.; Klene, M.; Adamo, C.; Cammi, R.; Ochterski, J. W.; Martin, R. L.; Morokuma, K.; Farkas, O.; Foresman, J. B.; Fox, D. J. Gaussian 16 . C.01. Gaussian Inc.: Wallingford, CT 2016.

(25) Ervin, K. M. Capture Collisions of Polyynide Anions with Hydrogen Atoms: Effect of the Ion Dipole, Quadrupole, and Anisotropic Polarizability. *Int. J. Mass Spectrom.* **2015**, *378*, 48–53. https://doi.org/10.1016/j.ijms.2014.07.009.

(26) Celli, F.; Weddle, G.; Ridge, D. P. On Statistical and Thermodynamic Approaches to Ion Polar Molecule Collisions. *J. Chem. Phys.* **1980**, *73*, 801–812. https://doi.org/10.1063/1.440187.

(27) Su, T.; Chesnavich, W. J. Parametrization of the Ion-Polar Molecule Collision Rate Constant by Trajectory Calculations. *J. Chem. Phys.* **1982**, *76*, 5183–5185. https://doi.org/10.1063/1.442828.

(28) Garcia, R. R.; Marsh, D. R.; Kinnison, D. E.; Boville, B. A.; Sassi, F. Simulation of Secular Trends in the Middle Atmosphere, 1950–2003. *J. Geophys. Res. Atmos.* **2007**, *112*. https://doi.org/https://doi.org/10.1029/2006JD007485.

(29) Lamarque, J.-F.; Emmons, L. K.; Hess, P. G.; Kinnison, D. E.; Tilmes, S.; Vitt, F.; Heald, C. L.; Holland, E. A.; Lauritzen, P. H.; Neu, J.; Orlando, J. J.; Rasch, P. J.; Tyndall, G. K. CAM-Chem: Description and Evaluation of Interactive Atmospheric Chemistry in the Community Earth System Model. *Geosci. Model Dev.* **2012**, *5*, 369–411. https://doi.org/10.5194/gmd-5-369-2012.

(30) Marsh, D. R.; Mills, M. J.; Kinnison, D. E.; Lamarque, J.-F.; Calvo, N.; Polvani, L. M. Climate Change from 1850 to 2005 Simulated in CESM1(WACCM). *J. Clim.* **2013**, *26*,

7372–7391. https://doi.org/https://doi.org/10.1175/JCLI-D-12-00558.1.

(31) Eyring, V.; Bony, S.; Meehl, G. A.; Senior, C. A.; Stevens, B.; Stouffer, R. J.; Taylor, K. E. Overview of the Coupled Model Intercomparison Project Phase 6 (CMIP6) Experimental Design and Organization. *Geosci. Model Dev.* **2016**, *9*, 1937–1958.

(32) Morgenstern, O.; Hegglin, M. I.; Rozanov, E.; O'Connor, F. M.; Abraham, N. L.; Akiyoshi, H.; Archibald, A. T.; Bekki, S.; Butchart, N.; Chipperfield, M. P.; Deushi, M.; Dhomse, S. S.; Garcia, R. R.; Hardiman, S. C.; Horowitz, L. W.; Jöckel, P.; Josse, B.; Kinnison, D.; Lin, M.; Mancini, E.; Manyin, M. E.; Marchand, M.; Marécal, V.; Michou, M.; Oman, L. D.; Pitari, G.; Plummer, D. A.; Revell, L. E.; Saint-Martin, D.; Schofield, R.; Stenke, A.; Stone, K.; Sudo, K.; Tanaka, T. Y.; Tilmes, S.; Yamashita, Y.; Yoshida, K.; Zeng, G. Review of the Global Models Used within Phase 1 of the Chemistry–Climate Model Initiative (CCMI). *Geosci. Model Dev.* **2017**, *10*, 639–671. https://doi.org/10.5194/gmd-10-639-2017.

(33) Orbe, C.; Plummer, D. A.; Waugh, D. W.; Yang, H.; Jöckel, P.; Kinnison, D. E.; Josse, B.; Marecal, V.; Deushi, M.; Abraham, N. L.; Archibald, A. T.; Chipperfield, M. P.; Dhomse, S.; Feng, W.; Bekki, S. Description and Evaluation of the Specified-Dynamics Experiment in the Chemistry-Climate Model Initiative . *Atmos. Chem. Phys.* **2020**, *20*, 3809–3840. https://doi.org/10.5194/acp-20-3809-2020.

(34) Cuevas, C. A.; Fernandez, R. P.; Kinnison, D. E.; Li, Q.; Lamarque, J.-F.; Trabelsi, T.; Francisco, J. S.; Solomon, S.; Saiz-Lopez, A. The Influence of Iodine on the Antarctic Stratospheric Ozone Hole. *Proc. Natl. Acad. Sci.* **2022**, *119*, e2110864119. https://doi.org/10.1073/pnas.2110864119.

(35) Molod, A.; Takacs, L.; Suarez, M.; Bacmeister, J. Development of the GEOS-5 Atmospheric General Circulation Model: Evolution from MERRA to MERRA2. *Geosci. Model Dev.* **2015**, *8*, 1339–1356. https://doi.org/10.5194/gmd-8-1339-2015.

(36) Li, Y.; Feng, W.; Plane, J. M. C.; Wang, T.; Chipperfield, M. P. The Impact of Rocket-Emitted Chlorine on Stratospheric Ozone. *Atmos. Chem. Phys.* **2026**, *26*, 3621–3635. https://doi.org/10.5194/acp-26-3621-2026.